

Article

Magnetized transonic accretion disks

Raj Kishor Joshi ¹*, Antonios Tsokaros ^{2,3,4}, Sanjit Debnath ⁵, Indranil Chattopadhyay ⁵, and Ramiz Aktar ⁶

¹ Nicolaus Copernicus Astronomical Center of the Polish Academy of Sciences, Bartycka 18, PL-00-716 Warsaw, Poland
² Department of Physics, University of Illinois at Urbana-Champaign, Urbana, Illinois 61801, USA
³ National Center for Supercomputing Applications, University of Illinois at Urbana-Champaign, Urbana, Illinois 61801, USA
⁴ Research Center for Astronomy and Applied Mathematics, Academy of Athens, Athens 11527, Greece
⁵ Aryabhatta Research Institute of Observational Sciences (ARIES), Manora Peak, Nainital 263001, India
⁶ Institute of Astronomy and Astrophysics, Academia Sinica, Taipei 10617, Taiwan, R.O.C.
* Correspondence: rjoshi@camk.edu.pl

Abstract: Theoretical studies of transonic accretion onto black holes reveal a wide range of possible solutions, broadly classified into smooth flows and flows featuring shocks. Accretion solutions that involve the formation of shocks are particularly intriguing, as they are expected to naturally produce observable variability features. However, despite their theoretical significance, time-dependent studies exploring the stability and evolution of such shocked solutions remain relatively scarce. To address this gap, we perform simulations of transonic accretion flows around a black hole in ideal magnetohydrodynamic framework. Our simulations are initialized using boundary conditions derived from semi-analytical hydrodynamical models, allowing us to explore the stability of these flows under varying magnetic field strengths. The presence of magnetic fields modifies the dynamics of the accretion flow through magnetic pressure, and the resulting force imbalance induces oscillations in the position of shock front. Our results show that variations in the emitted luminosity arising from shock oscillations appear as quasi-periodic oscillations (QPOs), a characteristic feature commonly observed in accreting black holes. We find that the QPO frequency is determined by the radial position of the shock front: oscillations occurring closer to the black hole produce frequencies of tens of hertz, whereas shocks located farther out yield sub-hertz frequencies.

Keywords: Black holes; Accretion; Numerical methods; Magnetohydrodynamics.

1. Introduction

Accretion onto compact objects such as black holes is one of the most fundamental processes governing high-energy astrophysical phenomena. The infall of matter into the deep gravitational potential well of a black hole releases enormous amounts of energy, which is often observed as intense radiation from accreting systems such as black hole X-ray binaries (BHXRBS) and active galactic nuclei (AGN) [1,2]. Understanding the physical mechanisms that regulate the structure, dynamics, and energetics of such accretion flows is therefore crucial for interpreting a broad range of high-energy astrophysical observations.

A key property of black hole accretion flows is their transonic nature: the flow must pass through one or more sonic points before crossing the event horizon [3–5]. Depending on the angular momentum of the accreting matter, two idealized limiting solutions can be identified. In the absence of angular momentum, the flow is spherically symmetric, leading to the classical Bondi accretion solution [3], where matter falls radially onto the compact object. In contrast, when the angular momentum is sufficiently high, the accreting material can settle into a geometrically thin, nearly Keplerian disk, in which radial motion is negligible and the flow is primarily rotational [1]. While these two extremes provide useful conceptual frameworks, realistic accretion flows around black holes are neither purely radial nor perfectly Keplerian.

In a more general scenario, rotating accretion flows with significant radial advection introduce a much richer dynamical structure through the interplay between centrifugal forces and advection velocities. The presence of angular momentum along with radial advection gives rise to the possibility of multiple sonic point regions where the flow velocity equals the local sound speed. Such transonic solutions are crucial for understanding the global structure of accretion flows, as they determine how matter can smoothly transition from subsonic to supersonic speeds while satisfying the inner boundary condition at the event horizon. The resulting flow topologies are diverse, ranging from single sonic point solutions similar to spherical Bondi accretion, to accretion flows that can exhibit multiple sonic points [6–8], which play a key role in regulating the thermodynamic and radiative properties of the accreting plasma.

Theoretical investigations of such transonic accretion flows have revealed that multiple critical points may form under specific combinations of flow parameters [6,9–11]. This multiplicity enables the formation of discontinuities, or standing shocks, where a portion of the bulk kinetic energy of the flow is converted into thermal energy [7,8,12–14]. The resulting hot, post-shock region can serve as a Comptonizing corona that upscatters soft photons, thereby influencing the observed emission spectrum of the accretion system [11,15,16]. Moreover, the time dependent nature of these shocks has been proposed as a mechanism to explain the variability and transient flaring often observed in accreting sources.

While analytical methods such as linear stability analysis provide a distinct approach to determine whether these solutions correspond to stable or unstable equilibrium configurations [17,18], capturing their complete dynamical evolution requires time-dependent numerical simulations. A series of inviscid hydrodynamic simulations have been performed to study the formation and evolution of shocked, transonic accretion disks [19–35]. Because shock formation is closely tied to the angular momentum distribution within the disk, the inclusion of viscosity, which governs angular momentum transport is expected to significantly influence both the existence and stability of the shock. Indeed, several studies have shown that viscosity can induce oscillations in shock position [10,36–43].

The characteristic frequencies of these oscillations are found to closely resemble the quasi-periodic oscillations (QPOs) observed in BHXRBS, suggesting that the underlying shock dynamics may provide a natural explanation for these observed luminosity modulations. Recent investigations by Debnath et al. [10,44] have further demonstrated that the temporal variations in luminosity arising from viscous, cooling-modulated shock oscillations can reproduce QPOs in the sub-Hertz to few-Hertz range for microquasars hosting black holes of tens of solar masses.

Magnetic fields are often present in accretion disks and can significantly influence their dynamics. Magnetic fields play a crucial role in driving angular momentum transport and energy dissipation through the magneto-rotational instability (MRI) [45,46]. The inclusion of magnetic fields introduces additional physical processes, such as magnetic pressure, tension, and reconnection, that can substantially alter the global accretion dynamics and the nature of shock formation. Despite the recognized importance of magnetic fields in shaping accretion dynamics, systematic investigations of transonic accretion flows with shocks in the magnetohydrodynamic (MHD) regime remain relatively scarce. Recent general relativistic magnetohydrodynamic (GRMHD) simulations by Mao et al. [34] and Di-hingia et al. [47] have shown that magnetized flows around rotating black holes can sustain standing shocks. Shock formation in accretion flows onto binary black hole systems has also been reported by Joshi et al. [48]. Although the number of such studies is still limited, they collectively demonstrate that shocks can also form in magnetized accretion flows. However, the role of magnetic field strength and topology in regulating the onset, stability, and oscillatory behavior of these shocks remains poorly constrained. Addressing these issues is crucial for developing a self-consistent framework that links the microphysics of magnetized accretion flows to the macroscopic variability observed in black hole systems. To bridge this gap, in this work, we present results from magnetohydrodynamic (MHD)

simulations of transonic accretion flows around a black hole, with an emphasis on the stability and temporal evolution of shock solutions. The simulations are initialized using boundary conditions derived from semi-analytical hydrodynamical solutions, which generate steady state shocks. Our objective is to investigate the time-dependent behavior of such solutions by analyzing the resulting flow morphology, evolution, and stability of shocks in the flow, and corresponding luminosity variations.

The remainder of the paper is organized as follows. Section 2 describes the theoretical framework and numerical setup used in our simulations. Section 4 presents the main results, focusing on the role of magnetic field strength in determining flow stability and shock dynamics. Finally, Section 6 summarizes our conclusions and outlines potential directions for future work.

2. Simulation Setup

We model the accretion flow using publicly available code PLUTO [49] in the ideal MHD limit. PLUTO uses higher-order Godunov scheme to solve the equations,

$$\frac{\partial \rho}{\partial t} + \nabla \cdot (\rho \mathbf{v}) = 0, \quad (1)$$

$$\frac{\partial(\rho \mathbf{v})}{\partial t} + \nabla \cdot (\rho \mathbf{v} \otimes \mathbf{v} - \mathbf{B} \otimes \mathbf{B}) + \nabla p_t = \rho \nabla \Phi_{PW}, \quad (2)$$

$$\frac{\partial \mathbf{B}}{\partial t} + \nabla \times (\mathbf{v} \times \mathbf{B}) = 0, \quad (3)$$

$$\frac{\partial E}{\partial t} + \nabla \cdot [(E + p_t) \mathbf{v} - (\mathbf{v} \cdot \mathbf{B}) \mathbf{B}] = \rho \mathbf{v} \cdot \nabla \Phi_{PW}, \quad (4)$$

here $\Phi_{PW} = -GM/(r - r_g)$ is the Paczyński-Wiita potential [50] and $r_g = 2GM/c^2$ is the Schwarzschild radius. $p_t = p + p_{mag}$ is the total pressure consisting of thermal (p), and magnetic ($p_{mag} = B^2/2$) pressure. The total energy density E is the sum of the internal, kinetic and magnetic energy density given as

$$E = e + \frac{1}{2}\rho|\mathbf{v}|^2 + \frac{|\mathbf{B}|^2}{2}, \quad (5)$$

In addition to the above equations the magnetic field satisfies the solenoidal constraint,

$$\nabla \cdot \mathbf{B} = 0. \quad (6)$$

To close the system of equations, an additional relation is required that connects the internal energy density e to the fluid variables ρ and p . We adopt an ideal gas equation of state (EoS) for which the internal energy density is given as $e = p/(\gamma - 1)$. The accreting matter is cold at large distances from the black hole and becomes progressively hotter as it approaches the event horizon. Consequently, the adiabatic index should transition from a higher value ($\gamma = 5/3$) in the outer, colder regions to a lower value ($\gamma = 4/3$) in the hotter inner regions. Accurately capturing this thermal evolution would require an EoS similar to the EoS given by Mathews [51], Ryu et al. [52], Chattopadhyay and Ryu [53] that self-consistently computes the adiabatic index from the local temperature. In the present study, such an equation of state was not incorporated into our simulation framework, and we therefore employed the fixed γ equation of state provided in PLUTO, adopting $\gamma = 4/3$.

These equations are solved on a spherical grid (r, θ, ϕ) using the HLLC Riemann solver [54] with piecewise parabolic reconstruction [55]. Time evolution is performed using a second-order Runge–Kutta (RK2) time-stepping method. To maintain the divergence-free condition of the magnetic field, we employ the hyperbolic divergence cleaning method of Dedner et al. [56].

We adopt a unit system in which the unit of length is the Schwarzschild radius, $r_g = 2GM/c^2$, and the velocity is measured in units of the speed of light, c . Hence, the unit of time is $t_g = 2GM/c^3$, where M is the mass of the black hole. In this unit system, the unit of specific angular momentum is

r_{gc} . Since our simulations do not include any dissipative processes, they are scale-free, and the length and time scales can be translated to those associated with either microquasars hosting stellar mass black holes or AGNs containing supermassive black holes, depending on the mass of the central object.

3. Numerical Framework: Initial and Boundary Conditions

The computational domain is initially filled with a tenuous, static atmosphere with a rest-mass density $\rho_{\text{atm}} = 10^{-5}$ and gas pressure $p_{\text{atm}} = 10^{-7}$. These parameters can be converted into physical units based on the specific value of mass accretion rate considered for the problem, as detailed in section 4.3. Matter is injected through the outer radial boundary; the injection parameters, the radial velocity v and the dimensionless temperature $\Theta \equiv p/\rho$ are taken from semi-analytical steady-state transonic solutions (see Debnath et al. 44 for details). The radial domain extends from $r = 1.8$ to $r = 200$. The inflow boundary condition is applied over an angular region $|\theta - \pi/2| \leq \pi/6$ at the outer radius, while the remainder of that boundary uses outflow (zero-gradient) boundary conditions. For 2D axisymmetric runs, we impose axisymmetric boundary conditions along the polar axis in θ . For 3D runs, we use polaraxis boundary condition available in PLUTO along the θ direction to avoid pole singularity. This boundary condition means copying the values to the ghost zones from the active zones after a rotation of π around the pole. The velocity components (except the parallel one) reverse sign. We use periodic boundary conditions along ϕ .

We used a grid resolution of $N_r \times N_\theta = 200 \times 296$ for 2D axisymmetric simulations and $N_r \times N_\theta \times N_\phi = 100 \times 296 \times 120$ for fully 3D run. The radial grid is logarithmically spaced to achieve higher resolution near the black hole. Additionally, the θ -grid has high resolution near the equator. The region $\pi/4 - 3\pi/4$ is resolved by 200 cells. The choice of resolution and grid structure was made to optimize the ability of code to capture shocks efficiently without incurring excessive computational cost. The resolution in the radial direction was tuned by matching the results of 1D simulation with analytical solution. For multi-dimensional simulations, the resolution along the θ direction also becomes important to capture a steady shock transition. We performed a series of numerical simulations for the unmagnetized flow to determine that a resolution of 100 cells in the region $\pi/2 \pm \pi/4$ is sufficient to capture a steady shock.

The magnetic field is prescribed as a purely poloidal configuration through a toroidal vector potential of the form

$$A_\phi(r, \theta) = A_0 r \sin \theta, \quad (7)$$

where A_0 is set to achieve the desired initial plasma beta,

$$\beta \equiv \frac{2p}{B^2}. \quad (8)$$

Different runs use different initial β values to explore the dependence of the flow on magnetic-field strength.

In order to avoid very small time steps caused by the unbounded nature of the Alfvén velocity in the non-relativistic MHD regime, we impose a ceiling on the magnetization parameter, defined as $\sigma = B^2/\rho$, with a threshold value of 100. We also set a floor value for the plasma β parameter at $\beta = 0.01$. Any cells exceeding these thresholds are flagged, and their values are reset to the prescribed limits. The simulations are evolved for long durations (typically $t \gtrsim 5 \times 10^4 t_g$, where $t_g \equiv 2GM/c^3$) to assess whether the system relaxes to a steady-state configuration or exhibits sustained time-dependent variability. The robustness of the numerical scheme and its ability to resolve shocks at the adopted resolution were verified by reproducing the corresponding one-dimensional solution, as presented in the Appendix A.

4. Results

We begin by presenting the results of the purely hydrodynamic simulation, which serves as the fiducial reference case for this study. This run establishes the baseline morphology of the shocked accretion flow and provides a benchmark for assessing deviations from the underlying steady-state analytical solution, ensuring that any departures can be attributed to genuine physical effects rather than numerical artifacts.

We then analyze the magnetized simulations, which display clear morphological differences relative to the hydrodynamic case, demonstrating the influence of magnetic fields on the accretion structure and the resulting time-dependent behavior. Finally, we computed the bolometric luminosities from all simulations through a posteriori radiative estimates, showing that the temporal evolution of the shocks produces a characteristic imprint on the emitted radiation.

4.1. Non-Magnetized Run

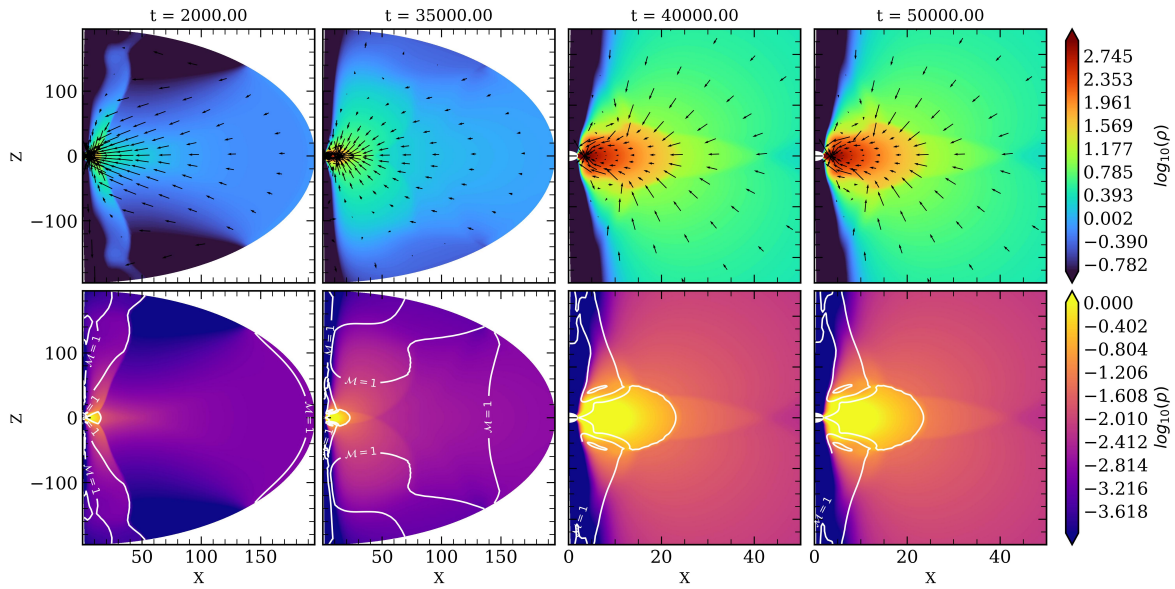


Figure 1. Top row: Density snapshots of the non-magnetized run M0. Arrows indicate the fluid velocity. Bottom row: Pressure snapshots with white contours indicating shock and sonic surfaces. Units of space and time are in terms of r_g and t_g correspondingly.

The fiducial simulation M0, is carried out under non-magnetized conditions. In this model, the accretion flow evolves solely under the influence of gravity and gas pressure. The solution is specified by a fixed angular momentum $\lambda = 1.75$ and a Bernoulli parameter $\mathcal{E} = 0.005$. Our simulation strategy for transonic accretion flows differs from approaches that employ Fishbone–Moncrief tori [57–59] or thin-disk initial conditions [5,60], where the computational domain is pre-filled with a prescribed disk profile. In contrast, for transonic flows, the domain is initially set to very low density and pressure floor values, and matter is continuously injected through the outer radial boundary. The injection parameters are taken directly from the analytical transonic solution, with $v_{\text{inj}} = -0.0198$ and $\Theta_{\text{inj}} = 0.00182$ at the outer boundary which is at $r_{\text{inj}} = 200$. The density at the outer boundary is set to $\rho = 1$, and v_ϕ is calculated using $v_\phi = \lambda / r_{\text{inj}}$.

In the top row of Fig. 1, we show logarithmic density contours overlaid with velocity vectors to illustrate the flow dynamics. The injected material initially takes some time to propagate inward and reach the inner boundary, as seen in the first panel. Once the inflow establishes itself, matter begins to accumulate and gradually settles into a steady configuration. The bottom row shows the

corresponding pressure distribution, with a contour indicating the surface where the Mach number $\mathcal{M} = v/c_s$ reaches unity, $c_s = \sqrt{\gamma\Theta}$ is the sound-speed. The chosen injection parameters impose a subsonic inflow at the outer boundary. As the gas moves inward under gravity, it accelerates and eventually becomes supersonic. At $t = 35000 t_g$, the contour $\mathcal{M} = 1$ identifies the sonic surface at approximately $r \sim 140$.

By $t = 40000 t_g$, sufficient amount of matter has accumulated to form a shock surface, with the shock located near $r \sim 25$ on the equatorial plane ($\theta = \pi/2$). The last two columns of the figure provide a zoomed-in view of the inner disk structure. A comparison between the snapshots at $t = 40000 t_g$ and $t = 50000 t_g$ demonstrates that the overall morphology approaches a quasi-steady state characterized by a well-defined standing shock. Although the one-dimensional analytical estimate predicts the shock location around $r \sim 10$, an exact match is not expected in multidimensional simulations, as additional degrees of freedom allow the Rankine–Hugoniot conditions [9] to be satisfied at different radii. The hydrodynamic run also exhibits clear equatorial symmetry about the mid-plane, consistent with the expected behavior of an axisymmetric accretion flow in the absence of perturbations [35].

4.2. Magnetized Simulations

We now turn to the magnetized simulations, which explore how varying magnetic field strengths affect the accretion dynamics. We initialize the flows with three different plasma β values: $\beta_0 = 10^3$, 5×10^4 , and 10^5 . The corresponding models, labeled M3, M4, and M5, are identical in all aspects except for this choice of initial magnetization.

As the steady shock solution is obtained by a perfect balance of forces in a pure hydrodynamic regime, a gradual departure from the steady state is expected if the magnetic field strength is increased. We start with model M5, the density contours with overlaid velocity vectors are plotted in the top row of Fig. 2, and plasma β is plotted in the bottom row.

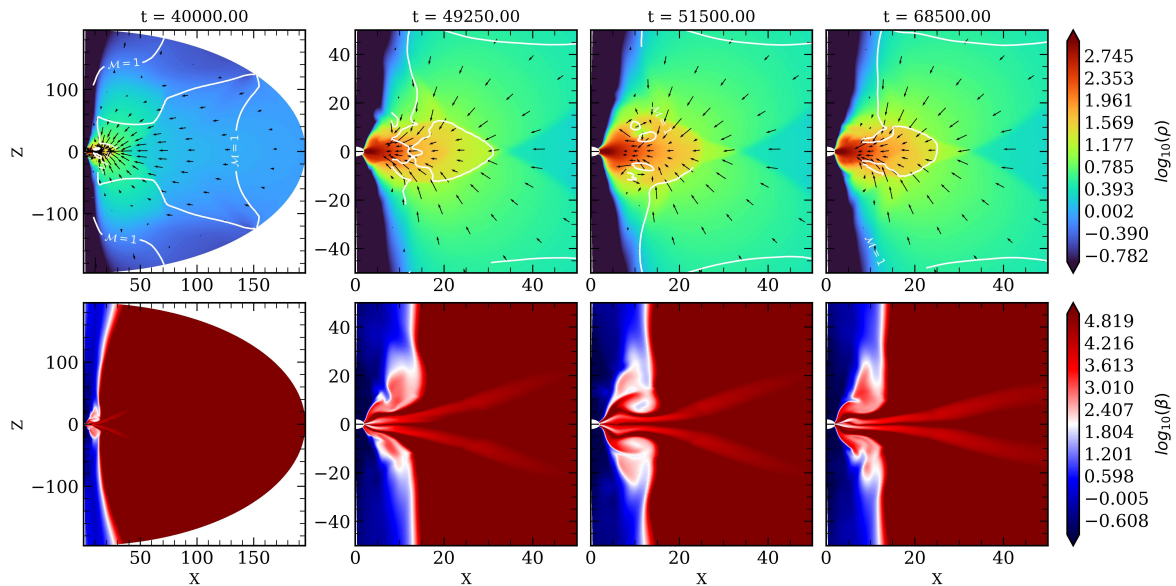


Figure 2. Density contours and distribution of plasma β for model M5.

The density distribution reveals subtle variations along the equatorial plane, indicating different stages of departure from perfect equatorial symmetry, which was observed for model M0. The influence of magnetic stresses on the flow dynamics is apparent on the shock location and structure of the post-shock region. The shock front exhibits mild distortions and asymmetry, particularly noticeable in the third column of Fig. 2. The corresponding plasma β distribution, shown in the bottom row, indicates that although the flow remains gas-pressure dominated ($\beta > 1$), the structure appears turbulent with

some voids of low-density regions in the post-shock disk. This is mainly attributed to the temporal behavior of the shock front. The magnetic field accumulated near the post-shock region tends to push the shock surface outward, while the inflowing matter exerts an opposing ram pressure that drives it inward toward the accreting center.

To illustrate how these competing effects contribute to the destabilization of the shock front, we examined the temporal evolution of the shock location on the equatorial plane, as shown in Fig. 3. The shock exhibits clear oscillatory behavior over time. For comparison, we also show the temporal variation of the shock front for model M0, in which the shock remains completely stable, displaying negligible changes in its position throughout the simulation.

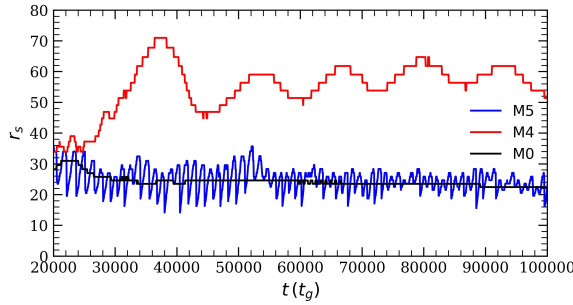


Figure 3. Temporal variation of the shock front position for different simulation runs, as indicated in the labels.

In model M4, the shock front is displaced farther out as shown in top panels of Fig. 4. The structure of the post-shock region differs noticeably from that in M1, with the mean shock location occurring at significantly larger radii. Additionally, a comparison with Figs. 2 and 1 shows that, in this case, the post-shock region becomes more vertically extended, even though the associated density jump is not particularly large. The bottom row shows that there are some regions confined close to the equatorial plane where plasma β reduces to the values of 1 – 10. The time series for the location of shock front plotted in Fig. 3 shows that the oscillation amplitude of the shock front increases, while the oscillation frequency decreases. This reduction in frequency is a consequence of the larger size of the post-shock region, which lengthens the dynamical timescale of the shock oscillations.

Finally, the evolution of model M3 with $\beta_0 = 10^3$, the morphology of the accretion flow undergoes a significant transformation, as shown in Fig. 5, we do not see the formation of a steady shock in this case. The magnetic field becomes dynamically dominant, and in the inner regions we see the formation of turbulent structures with lower plasma β . The equatorial symmetry seen in previous runs is largely disrupted, giving rise to asymmetric structures, as seen in the second and fourth columns of Fig. 5. Moreover, we observe that a fraction of the accreting matter is pushed outward from the vicinity of the black hole, a behavior primarily attributed to the enhanced magnetic pressure in the inner accretion region.

In Fig. 6, the angular momentum distribution is shown at different times for models M4 and M3. In model M3, we observe clear signatures of large-scale angular momentum transport away from the equatorial plane. Similar behavior was reported by Debnath et al. [10], where such redistribution was driven by viscous stresses within the disk. In contrast, model M4 shows no comparable large-scale vertical gradients; the angular momentum remains highest within a well-confined disk region. To check this, we also examined the MRI quality factor Q [61] for these models and confirmed that it is sufficiently resolved in M3 ($Q > 30$), whereas in M4 it remains lower ($Q < 10$ in the disk regions). The absence of extended angular momentum transport in M4 suggests that the magnetic field is not strong enough to drive significant angular-momentum transport, but the magnetic pressure and tension

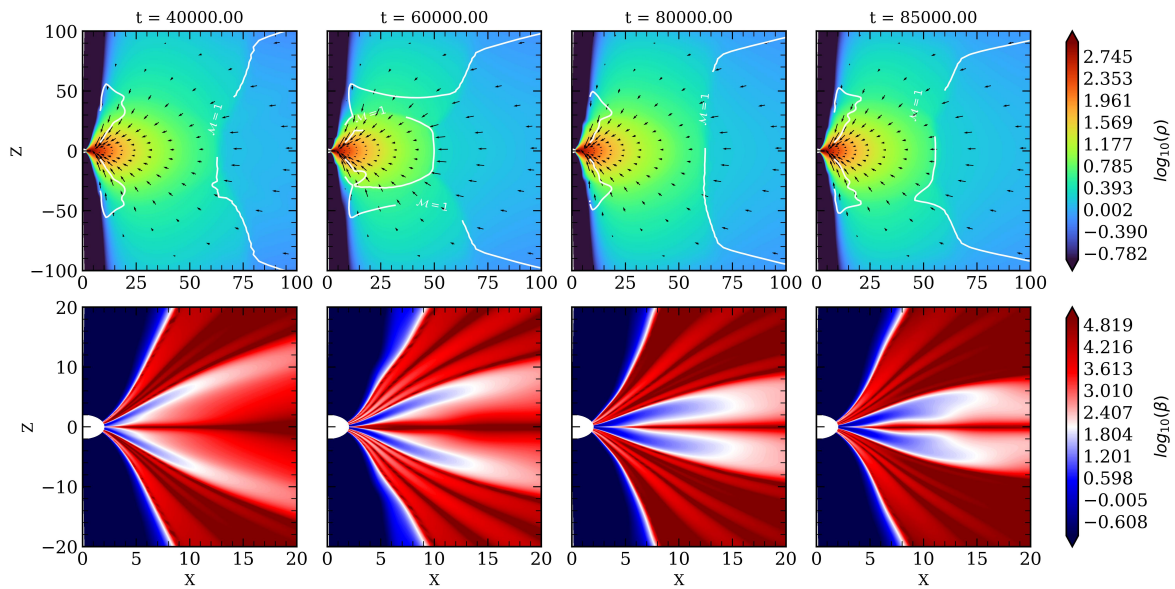


Figure 4. Same as Fig. 2 but for model M4.

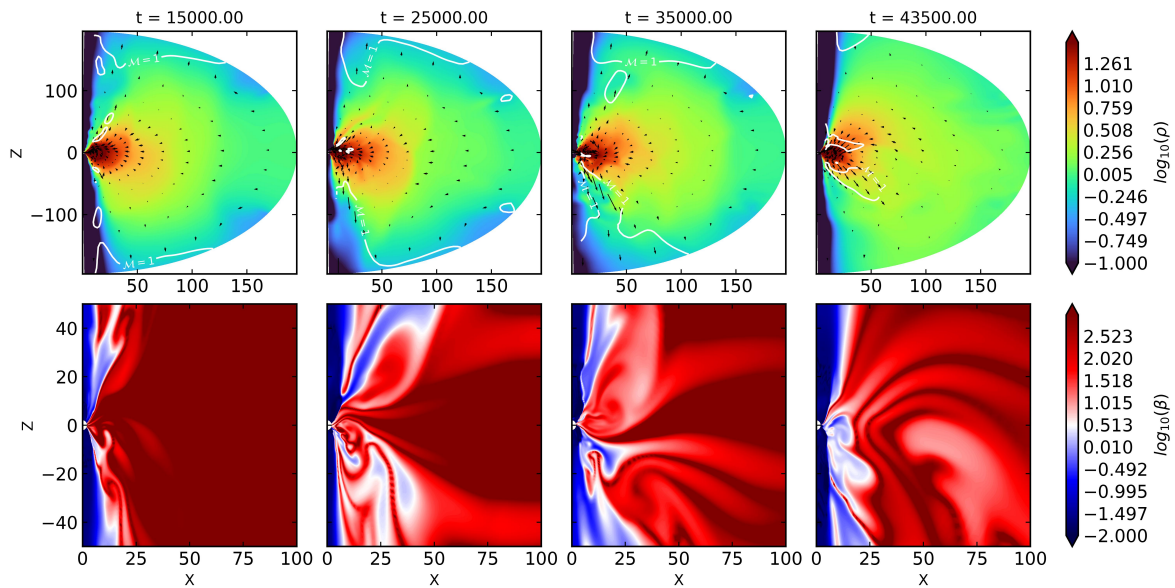


Figure 5. Same as Fig. 2 but for model M3.

forces are sufficient to introduce an imbalance in the net forces, which drives the observed shock oscillations.

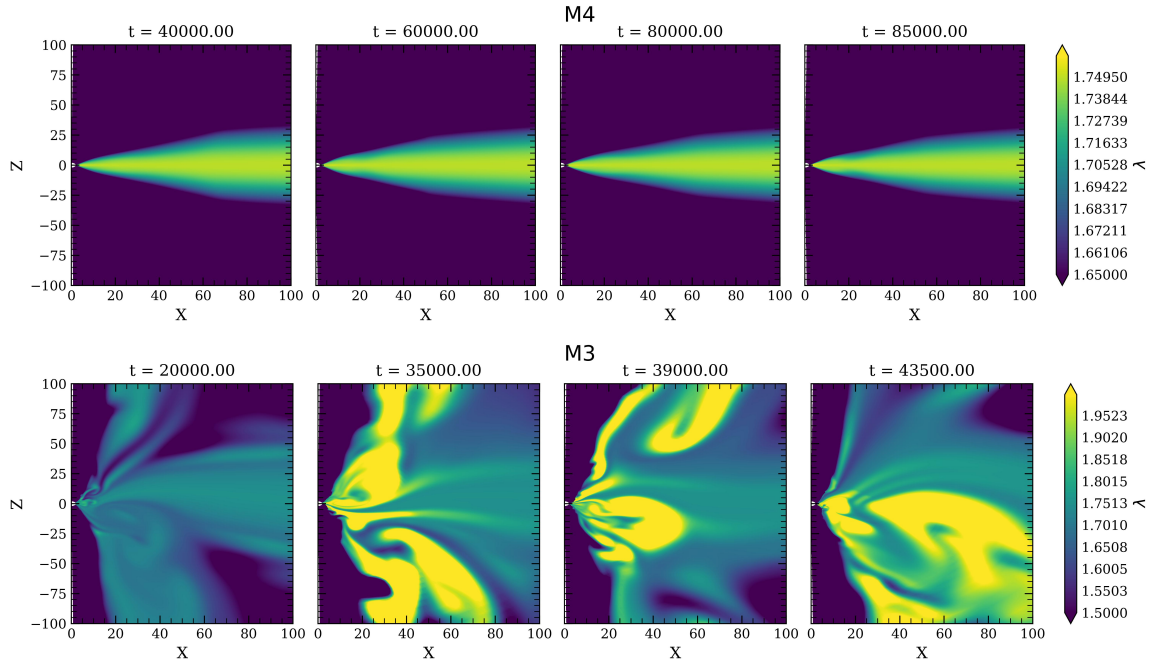


Figure 6. Snapshots of the angular momentum distribution for models M4 and M3.

4.3. Effect of shock oscillation

The post-shock region is hotter and denser in comparison to the pre-shock region, hence it emits high-energy photons [11]. The oscillations in shock location are expected to be reflected in the emitted radiation. We investigate this effect by analyzing the time series of luminosity calculated for different sets of simulations. We estimate the bremsstrahlung and synchrotron losses through a posteriori calculations as the representation of radiative processes in the accretion disk. The emissivity resulting from bremsstrahlung (measured in $\text{erg cm}^{-3} \text{ s}^{-1}$) is described by [5] and given as,

$$Q_{\text{br}} = 1.4 \times 10^{-27} n_e^2 \sqrt{T_e} \left(1 + 4.4 \times 10^{-10} T_e \right) \quad (9)$$

and the emissivity due to the synchrotron (in $\text{erg cm}^{-3} \text{ s}^{-1}$) is given by [62],

$$Q_{\text{syn}} = \frac{16}{3} \frac{e^2}{c} \left(\frac{eB}{m_e c} \right)^2 \Theta_e^2 n_e \quad (10)$$

At any time t , the total luminosity is the volume integral of the emissivities given as

$$L = \int (Q_{\text{syn}} + Q_{\text{br}}) dV \quad (11)$$

We obtain the luminosity profiles for a black hole mass, $M = 10M_{\odot}$. To calculate the density, we assume an accretion rate $\dot{M} = 0.1 M_{\text{Edd}}$, where $M_{\text{Edd}} = 1.44 \times 10^{17} (M/M_{\odot}) \text{ g/s}$ is the Eddington accretion rate. The density at the outer boundary (taken as $\rho = 1$ in code units) can be computed in physical units using the relation $\rho = \dot{M} / (4\pi v_{\text{inj}} r_{\text{inj}}^2 \cos\Delta)$, with Δ being the half angular extent of the disk.

The oscillatory behavior of the shock front is directly imprinted on the luminosity of the accretion flow. In the top panels of Fig. 7, we present the time evolution of the bolometric luminosity for models M5 (left) and M4 (right), with the corresponding power density spectra (PDS) shown in the lower panels.

Model M5 displays much more rapid luminosity fluctuations than M4, consistent with the faster shock oscillations in that model. A shock forming closer to the black hole heats the post-shock region more efficiently than one located farther out; thus, outward excursions of the shock naturally produce lower-luminosity phases, giving rise to the observed maxima and minima.

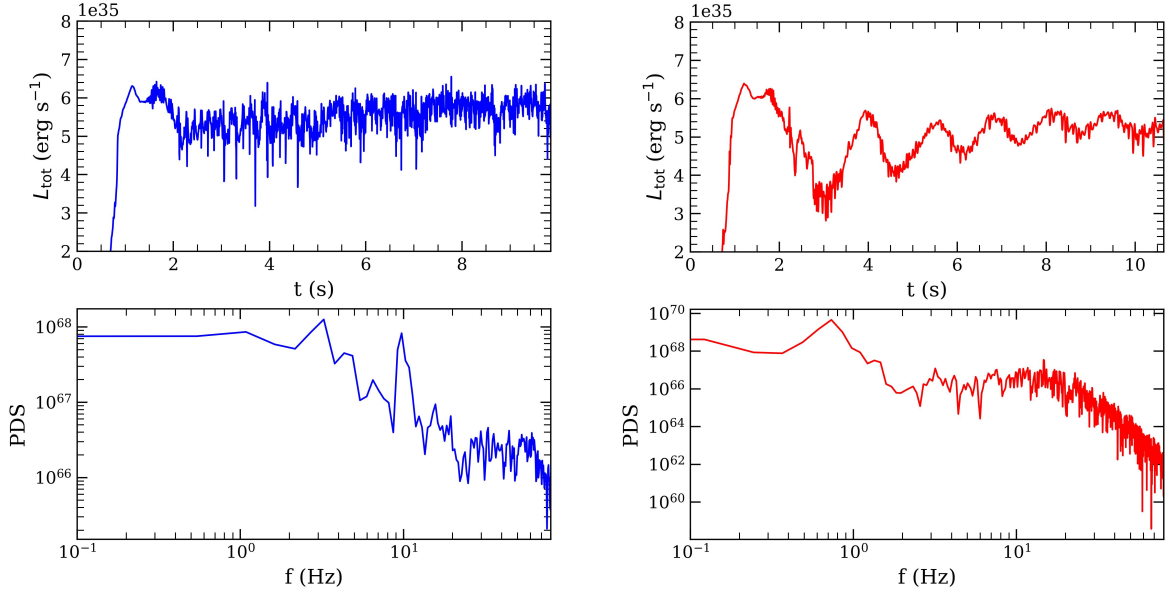


Figure 7. Time series of luminosity in units of (erg s $^{-1}$) and corresponding power spectra for model M5 (left column) and M4 (right column).

In model M4, the luminosity varies more slowly, with well-separated peaks and troughs, though small-scale fluctuations remain superimposed on the broader modulation. To identify QPOs associated with these variations, we computed the PDS of the luminosity signal, shown in the bottom panels. The PDS of M5 exhibits two prominent peaks near 10 Hz and 2 Hz. Additional features appear at 15 Hz and 18 Hz, but with power at least an order of magnitude lower than the low-frequency peaks. For model M4, the slower luminosity modulation produces a QPO at 0.75 Hz.

These results demonstrate that oscillating shock fronts can naturally generate QPOs over a range from sub-Hz to a few tens of Hz, depending on the mean location of the shock. Oscillations occurring closer to the black hole are faster and lead to rapid luminosity variations, whereas outwardly displaced shocks have longer dynamical timescales, reducing the characteristic oscillation frequency.

The time series of luminosity for model M3 is shown in Fig. 8. In this case, no steady shock forms throughout the simulation, and as a result, the bolometric luminosity remains noticeably lower than in models M4 and M5. This reduced emission reflects the absence of a persistent post-shock region capable of sustained heating. Although no stable shock is present, we do observe transient shock structures that momentarily appear in the flow and produce brief luminosity spikes. The bottom panel of Fig. 8 displays the radial profiles of Mach number and density, confirming the formation of these intermittent shocks; the corresponding spikes in luminosity are marked using matching colors. For comparison, profiles from epochs without any shock are also plotted, corresponding to the low-luminosity states.

Because these shock episodes are sporadic and short-lived, they fail to produce any coherent or quasi-periodic modulation. Consequently, the luminosity curve shows no well-defined oscillatory behavior. This outcome is fully consistent with expectations: in the absence of a stable shock oscillation region, the characteristic timescales required for QPO formation do not arise, leading instead to a predominantly low-luminosity, weakly variable state punctuated only by occasional, short-duration enhancements by a factor of 2–3.

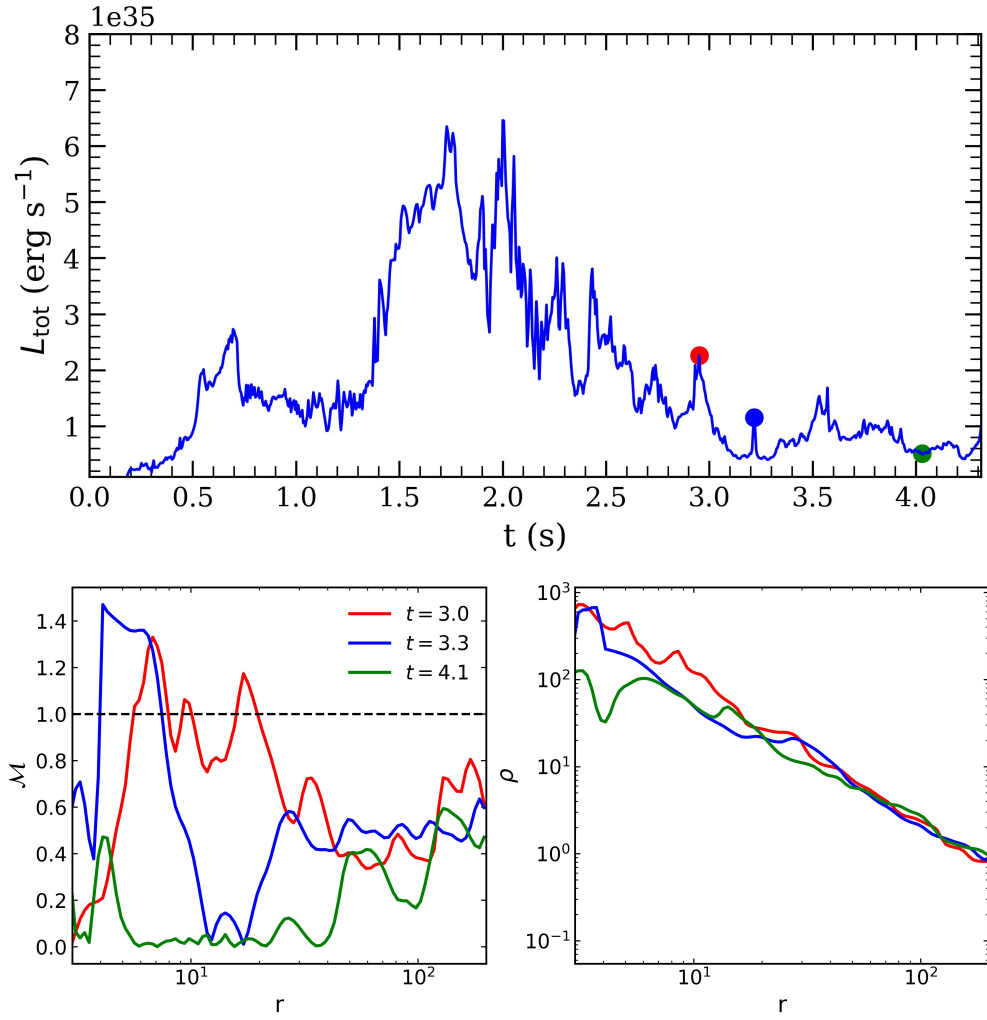


Figure 8. Variation of luminosity for M3 on top panel and bottom panels show equatorial plane profiles of Mach number and density plotted at time stamps mentioned in legend.

5. Three Dimensional Simulation

Recently, Garain and Kim [35] demonstrated that in three-dimensional simulations the post-shock region can develop a standing accretion shock instability (SASI), triggered under the influence of non-axisymmetric perturbations. Motivated by this result, we performed fully three-dimensional simulations for model M5. We do not impose any external perturbations as in our magnetized setup, the shock already undergoes intrinsic oscillations driven by magnetic pressure, which can naturally seed non-axisymmetric structure. Such features would be suppressed in two-dimensional simulations because of the enforced axisymmetric boundary conditions. The three-dimensional density structure, displayed at two separate time stamps, is shown in Fig. 9. The structure is visualized using slices taken at the planes $z = 0$ and $y = 0$. Due to the non-zero angular momentum of the flow, the region surrounding the polar axis contains very little matter. The density profiles shown at two different times indicate variations in the post-shock region, driven by oscillations of the shock front; however, the disk retains an overall symmetric structure.

The comparison of shock oscillation with the 2D run shown in Fig. 10 highlights that the oscillation frequency is almost similar but shock amplitude differs in comparison to 2D run.

We also calculate the effective viscosity parameter from Maxwell and Reynolds stresses.

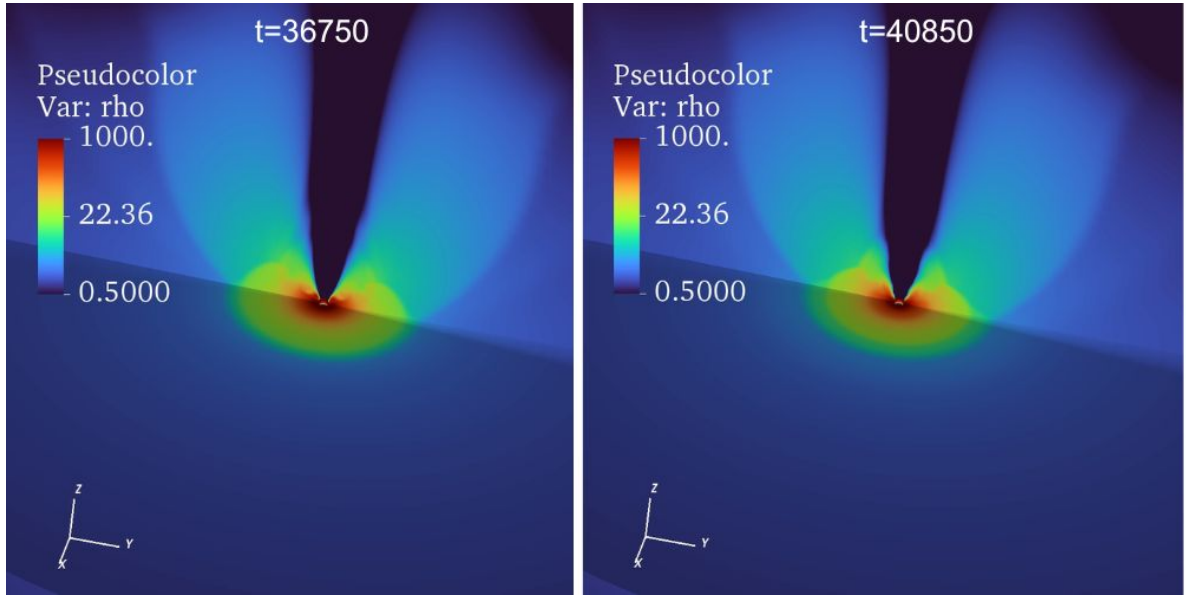


Figure 9. Density distribution for 3D M5 run.

The Reynolds stress is computed from velocity fluctuations:

$$T_{r\phi}^{\text{Reynolds}} = \rho v'_r v'_{\phi}, \quad (12)$$

where the fluctuating velocities are defined as

$$v'_r = v_r - \langle v_r \rangle_{\phi}, \quad v'_{\phi} = v_{\phi} - \langle v_{\phi} \rangle_{\phi}. \quad (13)$$

Here, $\langle \cdot \rangle_{\phi}$ denotes an azimuthal average at fixed (r, θ) .

The Maxwell stress is computed directly from the components of the magnetic field:

$$T_{r\phi}^{\text{Maxwell}} = - \frac{B_r B_{\phi}}{4\pi}. \quad (14)$$

The total $r\phi$ component of the stress is

$$T_{r\phi} = T_{r\phi}^{\text{Maxwell}} + T_{r\phi}^{\text{Reynolds}}, \quad (15)$$

and the Shakura–Sunyaev viscosity parameter is

$$\alpha_{ss} = \frac{T_{r\phi}}{P}. \quad (16)$$

To characterize radial profiles, we extract α , $T_{r\phi}^{\text{Maxwell}}$, and $T_{r\phi}^{\text{Reynolds}}$ along the equatorial plane ($\theta = \pi/2$). We further average over the azimuthal angle ϕ :

$$\alpha_{ss}(r) = \frac{1}{2\pi} \int_0^{2\pi} \alpha(r, \theta = \pi/2, \phi) d\phi, \quad (17)$$

The radial variation of α_{ss} is plotted in the right panel of Fig. 10. The Maximum value of α_{ss} is of the order of 10^{-2} . Since model M5 has a low magnetic field, the expected α values are relatively small. In contrast, models with higher magnetic fields, such as M3, exhibit more effective α , as their dynamical behavior resembles that of cases with higher viscosity, as discussed in [44]. Some negative spikes appear in the α distribution as a result of local turbulent fluctuations.

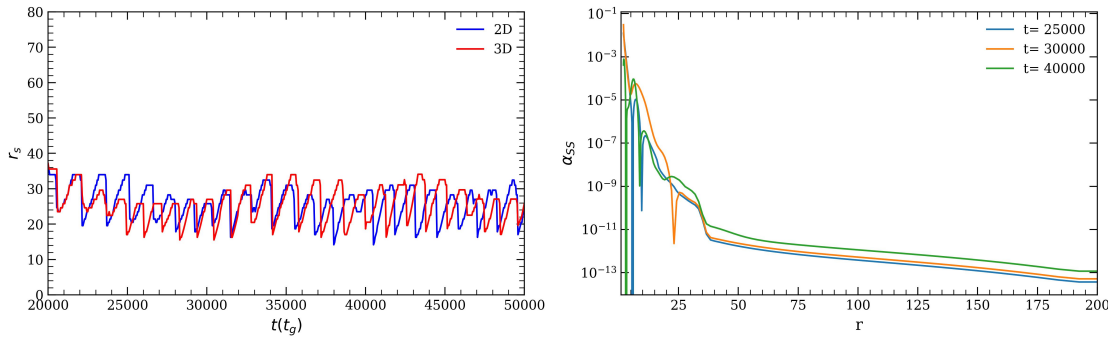


Figure 10. Left panel: Comparison between shock position in 2D and 3D run. Right panel shows radial variation of viscosity parameter.

6. Discussion and Conclusions

In this study, we explored the behavior of transonic accretion solutions in the magnetized regime. We performed ideal magnetohydrodynamic (MHD) simulations of accretion flows around a non-rotating black hole using a pseudo-Newtonian potential. The injection parameters for our simulations were derived from steady-state analytical transonic solutions, ensuring consistency between the numerical and analytical frameworks.

Our results demonstrate that accretion flows around black holes can form standing shock fronts as a consequence of the centrifugal barrier experienced by the inflowing matter. We then investigated the evolution of these shocked solutions under the influence of magnetic fields. By fixing the hydrodynamic parameters and systematically varying the magnetic field strength, we were able to study the effect of magnetic forces in a controlled manner. The introduction of magnetic fields produces significant modifications in the overall morphology and dynamics of the flow. Magnetic pressure and tension forces act to distort the shock surface, leading to a more irregular and time-dependent structure compared to the purely hydrodynamic case. Starting with very weak magnetic fields we showed that the global structure of the disk is preserved but the shock front starts to oscillate. As we increase the strength of the magnetic field, the magnetic pressure becomes comparable to the gas pressure, and the shock front exhibits fragmented behavior. The corresponding density and pressure distributions become increasingly asymmetric, indicating the development of magnetically driven instabilities.

Our results suggest that magnetic fields can destabilize an otherwise steady hydrodynamic shock configuration. Since the shock front compresses the inflowing matter and generates a hot, dense post-shock region, it naturally creates a boundary between the cold pre-shock and hot post-shock flow. Consequently, any temporal variations in the position or stability of the shock are expected to manifest as variability in the observed luminosity. This effect was reflected in the simulated bolometric luminosity, where temporal fluctuations trace either the periodic or the transient nature of the shocks, depending on the strength of the magnetic fields.

Although in this study we have used a pseudo-Newtonian potential to approximate the gravity of a non-rotating black hole, we expect the qualitative behavior of the flow to remain similar in the full general relativistic regime for a Schwarzschild black hole. The Paczyński–Wiita potential effectively captures a significant portion of the parameter space of transonic and shocked solutions when compared with fully relativistic treatments [7].

In the present study, we investigated the stability of shocked solutions by imposing a magnetic field on a flow obtained from a non-magnetized solution. However, analytical studies by Mitra and Das [63] have demonstrated that steady-state solutions can also be derived self-consistently within the GRMHD framework. For the future work, we plan to extend this study by including black hole rotation and full general relativistic magnetohydrodynamic (GRMHD) effects to account for frame-dragging and enhanced magnetic coupling near the event horizon.

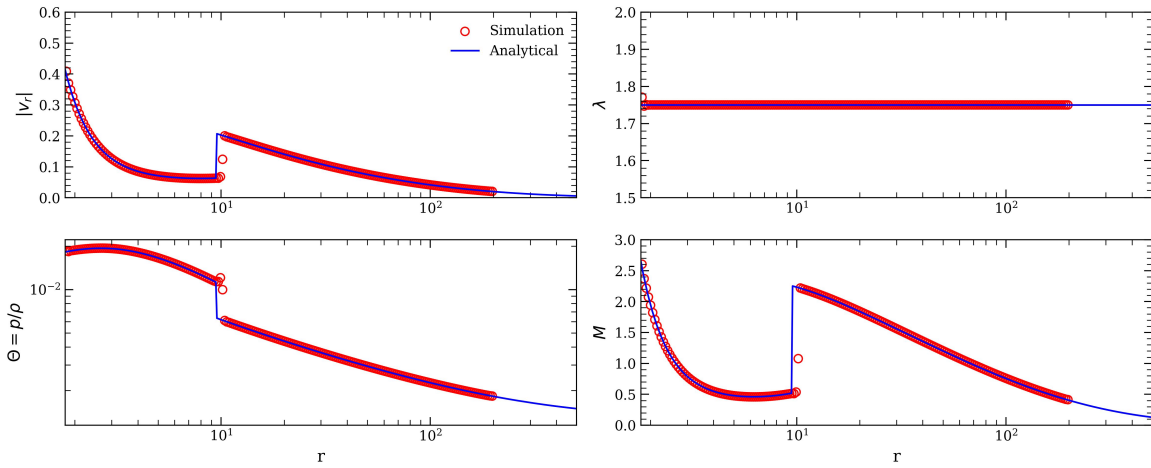


Figure A1. Comparison between one dimensional simulation and analytical solution.

Furthermore, incorporating radiative cooling processes and more realistic equations of state will allow a more direct connection between these simulations and observable properties, such as spectral variability and quasi-periodic oscillations (QPOs). Although, these effects are significant, they are beyond the scope of this study and will be explored in future work, with results to be reported separately.

Funding: This work was supported in part by National Science Foundation (NSF) Grants No. PHY-2308242 and No. OAC-2310548 to the University of Illinois at Urbana-Champaign. A.T. acknowledges support from the National Center for Supercomputing Applications (NCSA) at the University of Illinois at Urbana-Champaign through the NCSA Fellows program. This work used Anvil at Purdue University through allocation MCA99S008, from the Advanced Cyberinfrastructure Coordination Ecosystem: Services & Support (ACCESS) program, which is supported by National Science Foundation grants #2138259, #2138286, #2138307, #2137603, and #2138296. This research also used Frontera at TACC through allocation AST20025. Frontera is made possible by NSF award OAC-1818253. The initial computations and analysis for this article were conducted using the computer cluster at the Nicolaus Copernicus Astronomical Center of the Polish Academy of Sciences (CAMK PAN).

Informed Consent Statement: Not applicable

Data Availability Statement: The data underlying this article will be shared on reasonable request to the corresponding author.

Acknowledgments: R.K.J. would like to thank Miljenko Čemeljić for helpful comments during the preparation of this manuscript.

Conflicts of Interest: The authors declare no conflicts of interest.

Appendix A One dimensional simulation

In numerical simulations, the formation of shocks critically depends on the proper satisfaction of the Rankine–Hugoniot jump conditions. Since shocks inherently generate entropy, their correct capturing and resolution are sensitive to the numerical resolution. If the numerical dissipation is large the code will miss the shock jump. To determine an optimal setup, we performed a one-dimensional simulation aimed at reproducing the corresponding analytical solution. The results of this comparison are shown in Fig. A1, where we plot the radial profiles of the absolute radial velocity v_r , specific angular momentum λ , temperature $\Theta = p/\rho$, and Mach number. The simulation results correspond to a resolution of $N_r = 200$, which was adopted for all subsequent simulations. The comparison demonstrates that the shock is captured efficiently within approximately three grid cells. The code also preserves angular momentum very accurately. Although a minor discrepancy in the shock location is present but the solution was found to be stable.

Publisher's Note: The statements, opinions and data contained in all publications are solely those of the individual author(s) and contributor(s) and not of MDPI and/or the editor(s). MDPI and/or the editor(s) disclaim responsibility for any injury to people or property resulting from any ideas, methods, instructions or products referred to in the content.

- Shakura, N.I.; Sunyaev, R.A. Black holes in binary systems. Observational appearance. *A&A* **1973**, *24*, 337–355.
- Pringle, J.E.; Rees, M.J. Accretion Disc Models for Compact X-Ray Sources. *A&A* **1972**, *21*, 1.
- Bondi, H. On spherically symmetrical accretion. *MNRAS* **1952**, *112*, 195. <https://doi.org/10.1093/mnras/112.2.195>.
- Liang, E.P.T.; Thompson, K.A. Transonic disk accretion onto black holes. *ApJ* **1980**, *240*, 271–274. <https://doi.org/10.1086/158231>.
- Novikov, I.D.; Thorne, K.S. Astrophysics of black holes. In Proceedings of the Black Holes (Les Astres Occlus), 1973, pp. 343–450.
- Fukue, J. Transonic disk accretion revisited. *PASJ* **1987**, *39*, 309–327.
- Kumar, R.; Chattopadhyay, I. Dissipative advective accretion disc solutions with variable adiabatic index around black holes. *MNRAS* **2014**, *443*, 3444–3462, [arXiv:astro-ph.HE/1407.2130]. <https://doi.org/10.1093/mnras/stu1389>.
- Chattopadhyay, I.; Chakrabarti, S.K. Effects of the Composition on Transonic Properties of Accretion Flows around Black Holes. *International Journal of Modern Physics D* **2011**, *20*, 1597–1615, [arXiv:astro-ph.HE/1309.7900]. <https://doi.org/10.1142/S0218271811019487>.
- Chakrabarti, S.K. Standing Rankine-Hugoniot Shocks in the Hybrid Model Flows of the Black Hole Accretion and Winds. *ApJ* **1989**, *347*, 365. <https://doi.org/10.1086/168125>.
- Debnath, S.; Chattopadhyay, I.; Joshi, R.K. Oscillating shocks in the transonic viscous, variable Γ accretion flows around black holes. *MNRAS* **2024**, *528*, 3964–3980, [arXiv:astro-ph.HE/2401.07786]. <https://doi.org/10.1093/mnras/stae181>.
- Sarkar, S.; Chattopadhyay, I.; Laurent, P. Two-temperature solutions and emergent spectra from relativistic accretion discs around black holes. *A&A* **2020**, *642*, A209, [arXiv:astro-ph.HE/2007.00919]. <https://doi.org/10.1051/0004-6361/202037520>.
- Becker, P.A.; Das, S.; Le, T. Particle Acceleration and the Formation of Relativistic Outflows in Viscous Accretion Disks with Shocks. *ApJ* **2008**, *677*, L93, [arXiv:astro-ph.HE/0907.0872]. <https://doi.org/10.1086/588137>.
- Das, S.; Becker, P.A.; Le, T. Dynamical Structure of Viscous Accretion Disks with Shocks. *ApJ* **2009**, *702*, 649–659, [arXiv:astro-ph.HE/0907.0875]. <https://doi.org/10.1088/0004-637X/702/1/649>.
- Kumar, R.; Chattopadhyay, I. Estimation of the mass outflow rates from viscous accretion discs. *MNRAS* **2013**, *430*, 386–402, [arXiv:astro-ph.HE/1212.4231]. <https://doi.org/10.1093/mnras/sts641>.
- Chakrabarti, S.; Titarchuk, L.G. Spectral Properties of Accretion Disks around Galactic and Extragalactic Black Holes. *ApJ* **1995**, *455*, 623, [arXiv:astro-ph/astro-ph/9510005]. <https://doi.org/10.1086/176610>.
- Sarkar, S.; Singh, K.; Chattopadhyay, I.; Laurent, P. Two-temperature accretion flows around strongly magnetized stars and their spectral analysis. *MNRAS* **2023**, *522*, 3735–3752, [arXiv:astro-ph.HE/2304.03329]. <https://doi.org/10.1093/mnras/stad1064>.
- Nakayama, K. Hydrodynamic instability of accretion flows and wind flows with standing shock waves. *MNRAS* **1992**, *259*, 259–264. <https://doi.org/10.1093/mnras/259.2.259>.
- Nobuta, K.; Hanawa, T. Instability of Accretion Flow with a Shock Wave. *PASJ* **1994**, *46*, 257–265.
- Molteni, D.; Lanzafame, G.; Chakrabarti, S.K. Simulation of Thick Accretion Disks with Standing Shocks by Smoothed Particle Hydrodynamics. *ApJ* **1994**, *425*, 161, [arXiv:astro-ph/astro-ph/9310047]. <https://doi.org/10.1086/173972>.
- Molteni, D.; Sponholz, H.; Chakrabarti, S.K. Resonance Oscillation of Radiative Shock Waves in Accretion Disks around Compact Objects. *ApJ* **1996**, *457*, 805, [arXiv:astro-ph/astro-ph/9508022]. <https://doi.org/10.1086/176775>.
- Molteni, D.; Ryu, D.; Chakrabarti, S.K. Numerical Simulations of Standing Shocks in Accretion Flows around Black Holes: A Comparative Study. *ApJ* **1996**, *470*, 460, [arXiv:astro-ph/astro-ph/9605116]. <https://doi.org/10.1086/177877>.

22. Ryu, D.; Brown, G.L.; Ostriker, J.P.; Loeb, A. Stable and Unstable Accretion Flows with Angular Momentum near a Point Mass. *ApJ* **1995**, *452*, 364, [[arXiv:astro-ph/astro-ph/9504004](https://arxiv.org/abs/astro-ph/9504004)]. <https://doi.org/10.1086/176308>.
23. Giri, K.; Chakrabarti, S.K.; Samanta, M.M.; Ryu, D. Hydrodynamic simulations of oscillating shock waves in a sub-Keplerian accretion flow around black holes. *MNRAS* **2010**, *403*, 516–524, [[arXiv:astro-ph.HE/0912.1174](https://arxiv.org/abs/astro-ph.HE/0912.1174)]. <https://doi.org/10.1111/j.1365-2966.2009.16147.x>.
24. Okuda, T.; Molteni, D. Low angular momentum flow model for Sgr A*. *MNRAS* **2012**, *425*, 2413–2421, [[arXiv:astro-ph.HE/1206.5338](https://arxiv.org/abs/astro-ph.HE/1206.5338)]. <https://doi.org/10.1111/j.1365-2966.2012.21571.x>.
25. Garain, S.K.; Ghosh, H.; Chakrabarti, S.K. Effects of Compton Cooling on Outflow in a Two-component Accretion Flow around a Black Hole: Results of a Coupled Monte Carlo Total Variation Diminishing Simulation. *ApJ* **2012**, *758*, 114, [[arXiv:astro-ph.HE/1210.3515](https://arxiv.org/abs/astro-ph.HE/1210.3515)]. <https://doi.org/10.1088/0004-637X/758/2/114>.
26. Garain, S.K.; Ghosh, H.; Chakrabarti, S.K. Quasi-periodic oscillations in a radiative transonic flow: results of a coupled Monte Carlo-TVD simulation. *MNRAS* **2014**, *437*, 1329–1336, [[arXiv:astro-ph.HE/1310.6493](https://arxiv.org/abs/astro-ph.HE/1310.6493)]. <https://doi.org/10.1093/mnras/stt1969>.
27. Suková, P.; Charzyński, S.; Janiuk, A. Shocks in the relativistic transonic accretion with low angular momentum. *MNRAS* **2017**, *472*, 4327–4342, [[arXiv:astro-ph.HE/1709.01824](https://arxiv.org/abs/astro-ph.HE/1709.01824)]. <https://doi.org/10.1093/mnras/stx2254>.
28. Kim, J.; Garain, S.K.; Balsara, D.S.; Chakrabarti, S.K. General relativistic numerical simulation of sub-Keplerian transonic accretion flows on to black holes: Schwarzschild space-time. *MNRAS* **2017**, *472*, 542–549, [[arXiv:astro-ph.HE/1707.09856](https://arxiv.org/abs/astro-ph.HE/1707.09856)]. <https://doi.org/10.1093/mnras/stx1986>.
29. Kim, J.; Garain, S.K.; Chakrabarti, S.K.; Balsara, D.S. General relativistic numerical simulation of sub-Keplerian transonic accretion flows on to rotating black holes: Kerr space-time. *MNRAS* **2019**, *482*, 3636–3645, [[arXiv:astro-ph.HE/1810.12469](https://arxiv.org/abs/astro-ph.HE/1810.12469)]. <https://doi.org/10.1093/mnras/sty2953>.
30. Palit, I.; Janiuk, A.; Czerny, B. Clumpy Wind Accretion in Cygnus X-1. *ApJ* **2020**, *904*, 21, [[arXiv:astro-ph.HE/2009.09121](https://arxiv.org/abs/astro-ph.HE/2009.09121)]. <https://doi.org/10.3847/1538-4357/abba1b>.
31. Okuda, T.; Singh, C.B.; Aktar, R. Radiative shock oscillation model for the long-term flares of Sgr A*. *MNRAS* **2022**, *514*, 5074–5084, [[arXiv:astro-ph.HE/2206.04919](https://arxiv.org/abs/astro-ph.HE/2206.04919)]. <https://doi.org/10.1093/mnras/stac1630>.
32. Olivares, H.R.; Mościbrodzka, M.A.; Porth, O. General relativistic hydrodynamic simulations of perturbed transonic accretion. *A&A* **2023**, *678*, A141, [[arXiv:astro-ph.HE/2301.12020](https://arxiv.org/abs/astro-ph.HE/2301.12020)]. <https://doi.org/10.1051/0004-6361/202346010>.
33. Kwan, T.M.; Dai, L.; Tchekhovskoy, A. The Effects of Gas Angular Momentum on the Formation of Magnetically Arrested Disks and the Launching of Powerful Jets. *ApJ* **2023**, *946*, L42, [[arXiv:astro-ph.HE/2211.12726](https://arxiv.org/abs/astro-ph.HE/2211.12726)]. <https://doi.org/10.3847/2041-8213/acc334>.
34. Mao, J.; Dihingia, I.K.; Mizuno, Y.; Nagataki, S. Low-angular-momentum Black Hole Accretion: First General Relativistic Magnetohydrodynamic Evidence of Standing Shocks. *ApJ* **2025**, *990*, 12. <https://doi.org/10.3847/1538-4357/adf635>.
35. Garain, S.K.; Kim, J. Three-dimensional simulations of advective, sub-Keplerian accretion flow on to non-rotating black holes. *MNRAS* **2023**, *519*, 4550–4563, [[arXiv:astro-ph.HE/2212.08310](https://arxiv.org/abs/astro-ph.HE/2212.08310)]. <https://doi.org/10.1093/mnras/stac3736>.
36. Lanzaflame, G.; Molteni, D.; Chakrabarti, S.K. Smoothed particle hydrodynamic simulations of viscous accretion discs around black holes. *MNRAS* **1998**, *299*, 799–804, [[arXiv:astro-ph/astro-ph/9706248](https://arxiv.org/abs/astro-ph/9706248)]. <https://doi.org/10.1046/j.1365-8711.1998.01816.x>.
37. Lee, S.J.; Ryu, D.; Chattpadhyay, I. Quasi-spherical, Time-dependent Viscous Accretion Flow: One-dimensional Results. *ApJ* **2011**, *728*, 142, [[arXiv:astro-ph.CO/1012.4548](https://arxiv.org/abs/astro-ph.CO/1012.4548)]. <https://doi.org/10.1088/0004-637X/728/2/142>.
38. Giri, K.; Chakrabarti, S.K. Hydrodynamic simulations of viscous accretion flows around black holes. *MNRAS* **2012**, *421*, 666–678, [[arXiv:astro-ph.HE/1112.1500](https://arxiv.org/abs/astro-ph.HE/1112.1500)]. <https://doi.org/10.1111/j.1365-2966.2011.20343.x>.
39. Giri, K.; Chakrabarti, S.K. Hydrodynamic simulation of two-component advective flows around black holes. *MNRAS* **2013**, *430*, 2836–2843, [[arXiv:astro-ph.HE/1212.6493](https://arxiv.org/abs/astro-ph.HE/1212.6493)]. <https://doi.org/10.1093/mnras/stt087>.
40. Das, S.; Chattpadhyay, I.; Nandi, A.; Molteni, D. Periodic mass loss from viscous accretion flows around black holes. *MNRAS* **2014**, *442*, 251–258, [[arXiv:astro-ph.HE/1405.4415](https://arxiv.org/abs/astro-ph.HE/1405.4415)]. <https://doi.org/10.1093/mnras/stu864>.
41. Giri, K.; Garain, S.K.; Chakrabarti, S.K. Segregation of a Keplerian disc and sub-Keplerian halo from a transonic flow around a black hole by viscosity and cooling processes. *MNRAS* **2015**, *448*, 3221–3228, [[arXiv:astro-ph.HE/1502.00455](https://arxiv.org/abs/astro-ph.HE/1502.00455)]. <https://doi.org/10.1093/mnras/stv223>.

42. Okuda, T.; Das, S. Unstable mass-outflows in geometrically thick accretion flows around black holes. *MNRAS* **2015**, *453*, 147–156, [[arXiv:astro-ph/1507.04326](https://arxiv.org/abs/astro-ph/1507.04326)]. <https://doi.org/10.1093/mnras/stv1626>.
43. Lee, S.J.; Chattopadhyay, I.; Kumar, R.; Hyung, S.; Ryu, D. Simulations of Viscous Accretion Flow around Black Holes in a Two-dimensional Cylindrical Geometry. *ApJ* **2016**, *831*, 33, [[arXiv:astro-ph/1608.03997](https://arxiv.org/abs/astro-ph/1608.03997)]. <https://doi.org/10.3847/0004-637X/831/1/33>.
44. Debnath, S.; Chattopadhyay, I.; Joshi, R.K.; Laurent, P.; Tripathi, P.K.; Khan, M.S. Dynamical Properties of Oscillating, Viscous, Transonic Accretion Disks around Black Holes. *ApJ* **2025**, *994*, 48, [[arXiv:astro-ph/2509.19934](https://arxiv.org/abs/astro-ph/2509.19934)]. <https://doi.org/10.3847/1538-4357/ae0ca7>.
45. Balbus, S.A.; Hawley, J.F. A Powerful Local Shear Instability in Weakly Magnetized Disks. I. Linear Analysis. *ApJ* **1991**, *376*, 214. <https://doi.org/10.1086/170270>.
46. Hawley, J.F.; Balbus, S.A. A Powerful Local Shear Instability in Weakly Magnetized Disks. III. Long-Term Evolution in a Shearing Sheet. *ApJ* **1992**, *400*, 595. <https://doi.org/10.1086/172021>.
47. Dihingia, I.K.; Uniyal, A.; Mizuno, Y. The Fate of Transonic Shocks around Black Holes and their Future Astrophysical Implications. *arXiv e-prints* **2025**, p. arXiv:2507.23187, [[arXiv:astro-ph/2507.23187](https://arxiv.org/abs/2507.23187)]. <https://doi.org/10.48550/arXiv.2507.23187>.
48. Joshi, R.K.; Bhake, A.; Banerjee, B.; Vaidya, B.; Ruiz, M.; Tsokaros, A.; Mignone, A.; Branchesi, M.; Shukla, A.; Čemeljić, M. Binary black holes in magnetized AGN disks. *arXiv e-prints* **2025**, p. arXiv:2509.16796, [[arXiv:astro-ph/2509.16796](https://arxiv.org/abs/2509.16796)]. <https://doi.org/10.48550/arXiv.2509.16796>.
49. Mignone, A.; Bodo, G.; Massaglia, S.; Matsakos, T.; Tesileanu, O.; Zanni, C.; Ferrari, A. PLUTO: A Numerical Code for Computational Astrophysics. *ApJS* **2007**, *170*, 228–242, [[arXiv:astro-ph/0701854](https://arxiv.org/abs/astro-ph/0701854)]. <https://doi.org/10.1086/513316>.
50. Paczyński, B.; Wiita, P.J. Thick Accretion Disks and Supercritical Luminosities. *A&A* **1980**, *88*, 23.
51. Mathews, W.G. The Hydromagnetic Free Expansion of a Relativistic Gas. *ApJ* **1971**, *165*, 147. <https://doi.org/10.1086/150883>.
52. Ryu, D.; Chattopadhyay, I.; Choi, E. Equation of State in Numerical Relativistic Hydrodynamics. *ApJS* **2006**, *166*, 410–420, [[arXiv:astro-ph/0605550](https://arxiv.org/abs/astro-ph/0605550)]. <https://doi.org/10.1086/505937>.
53. Chattopadhyay, I.; Ryu, D. Effects of Fluid Composition on Spherical Flows Around Black Holes. *ApJ* **2009**, *694*, 492–501, [[arXiv:astro-ph/0812.2607](https://arxiv.org/abs/0812.2607)]. <https://doi.org/10.1088/0004-637X/694/1/492>.
54. Harten, A.; Lax, P.D.; Leer, B.v. On Upstream Differencing and Godunov-Type Schemes for Hyperbolic Conservation Laws. *SIAM Review* **1983**, *25*, 35–61, [<https://doi.org/10.1137/1025002>]. <https://doi.org/10.1137/1025002>.
55. Colella, P.; Woodward, P.R. The Piecewise Parabolic Method (PPM) for Gas-Dynamical Simulations. *Journal of Computational Physics* **1984**, *54*, 174–201. [https://doi.org/10.1016/0021-9991\(84\)90143-8](https://doi.org/10.1016/0021-9991(84)90143-8).
56. Dedner, A.; Kemm, F.; Kröner, D.; Munz, C.D.; Schnitzer, T.; Wesenberg, M. Hyperbolic Divergence Cleaning for the MHD Equations. *Journal of Computational Physics* **2002**, *175*, 645–673. <https://doi.org/10.1006/jcph.2001.6961>.
57. Fishbone, L.G.; Moncrief, V. Relativistic fluid disks in orbit around Kerr black holes. *ApJ* **1976**, *207*, 962–976. <https://doi.org/10.1086/154565>.
58. Aktar, R.; Pan, K.C.; Okuda, T. Radiation RMHD Accretion Flows around Spinning AGNs: A Comparative Study of MAD and SANE State. *ApJ* **2024**, *972*, 18, [[arXiv:astro-ph/2406.10496](https://arxiv.org/abs/astro-ph/2406.10496)]. <https://doi.org/10.3847/1538-4357/ad5a8a>.
59. Aktar, R.; Pan, K.C.; Okuda, T. Evolution of MHD torus and mass outflow around spinning AGNs. *MNRAS* **2024**, *527*, 1745–1759, [[arXiv:astro-ph/2310.15501](https://arxiv.org/abs/astro-ph/2310.15501)]. <https://doi.org/10.1093/mnras/stad3287>.
60. Mishra, B.; Begelman, M.C.; Armitage, P.J.; Simon, J.B. Strongly magnetized accretion discs: structure and accretion from global magnetohydrodynamic simulations. *MNRAS* **2020**, *492*, 1855–1868, [[arXiv:astro-ph/1907.08995](https://arxiv.org/abs/astro-ph/1907.08995)]. <https://doi.org/10.1093/mnras/stz3572>.
61. Sano, T.; Inutsuka, S.i.; Turner, N.J.; Stone, J.M. Angular Momentum Transport by Magnetohydrodynamic Turbulence in Accretion Disks: Gas Pressure Dependence of the Saturation Level of the Magnetorotational Instability. *ApJ* **2004**, *605*, 321–339, [[arXiv:astro-ph/0312480](https://arxiv.org/abs/astro-ph/0312480)]. <https://doi.org/10.1086/382184>.
62. Shapiro, S.L.; Teukolsky, S.A. Book-Review - Black-Holes White Dwarfs and Neutron Stars. *Journal of the British Astronomical Association* **1983**, *93*, 276.
63. Mitra, S.; Das, S. Low-angular-momentum General Relativistic Magnetohydrodynamic Accretion Flows around Rotating Black Holes with Shocks. *ApJ* **2024**, *971*, 28, [[arXiv:astro-ph/2405.16326](https://arxiv.org/abs/astro-ph/2405.16326)]. <https://doi.org/10.3847/1538-4357/ad55cb>.